

Review

# Modeling Nearby Low-Luminosity Active-Galactic-Nucleus Jet Images at All VLBI Scales

Hung-Yi Pu <sup>1,2,3,4,\*</sup> , Keiichi Asada <sup>2</sup>  and Masanori Nakamura <sup>2,5</sup> 

<sup>1</sup> Department of Physics, National Taiwan Normal University, No. 88, Sec. 4, Tingzhou Rd., Taipei 116, Taiwan

<sup>2</sup> Institute of Astronomy and Astrophysics, Academia Sinica, 11F of Astronomy-Mathematics Building, AS/NTU No. 1, Sec. 4, Roosevelt Rd., Taipei 10617, Taiwan

<sup>3</sup> Center of Astronomy and Gravitation, National Taiwan Normal University, No. 88, Sec. 4, Tingzhou Rd., Taipei 116, Taiwan

<sup>4</sup> Physics Division, National Center for Theoretical Sciences, Taipei 10617, Taiwan

<sup>5</sup> Department of General Science and Education, National Institute of Technology, Hachinohe College, 16-1 Uwanotai, Tamonoki, Hachinohe City 039-1192, Aomori, Japan

\* Correspondence: hypu@gapps.ntnu.edu.tw

**Abstract:** Relativistic jets from nearby low-luminosity active-galactic-nuclei (LLAGN) were observed by Very-Long Baseline Interferometry (VLBI) across many orders of magnitude in space, from milliparsec to sub-parsec scales, and from the jet base in the vicinity of black holes to the jet collimation and acceleration regions. With the improved resolution for VLBI observations, resolved VLBI jet morphologies provide valuable opportunities for testing and constraining black hole jet physics. In this review, we summarize and discuss the current progress of modeling nearby LLAGN jet images from horizon scales to large scales, including the construction of jet models and the assumed emission details. Illustrative examples for jet image modeling are also given to demonstrate how jet image features may vary with the underlying physics.

**Keywords:** black holes; relativistic jet; magnetohydrodynamics; active galaxies



**Citation:** Pu, H.-Y.; Asada, K.;

Nakamura, M. Modeling Nearby

Low-Luminosity

Active-Galactic-Nucleus Jet Images at

All VLBI Scales. *Galaxies* **2022**, *10*, 104.

[https://doi.org/10.3390/](https://doi.org/10.3390/galaxies10060104)

[galaxies10060104](https://doi.org/10.3390/galaxies10060104)

Academic Editor: Junhui Fan

Received: 1 September 2022

Accepted: 3 October 2022

Published: 25 October 2022

**Publisher's Note:** MDPI stays neutral with regard to jurisdictional claims in published maps and institutional affiliations.



**Copyright:** © 2022 by the authors. Licensee MDPI, Basel, Switzerland. This article is an open access article distributed under the terms and conditions of the Creative Commons Attribution (CC BY) license (<https://creativecommons.org/licenses/by/4.0/>).

## 1. Introduction

Very-Long Baseline Interferometry (VLBI) observations have provided a wealth of information regarding the innermost radio jets of nearby low-luminosity AGN (LLAGN) systems, from event horizon scale ( $\sim 1R_g \equiv GM_{\text{BH}}/c^2$ ) to  $\sim$ sub-parsec scale ( $\sim M_{\text{BH}}/M_{\odot} \times 10^{13} R_g$ ) (e.g., [1–12]). For a supermassive black hole with  $10^{8-9} M_{\odot}$ , parsec scale corresponds to  $10^{4-5} R_g$ , roughly within the Bondi radius ( $10^{5-6} R_g$ ). Beyond such scale, e.g., kiloparsec or even megaparsec, a jet's interaction with their surroundings is expected, resulting in lobes, deceleration, recollimation, changing of geometry, etc., and, therefore, the additional complexity of their modeling should be considered (e.g., [13,14]).

Observed spectra from black hole accretion jet systems include the contribution from both the accretion and the jet. The spectra of LLAGN are usually featured with a near millimeter bump ( $\sim 10^2$  GHz) [15–18], which is usually referred to as the thermal synchrotron emission contributed by the innermost region of a radiatively inefficient accretion flow (RIAF), a type of black hole accretion at a low accretion rate ( $\dot{M} < 0.01\dot{M}_{\text{Edd}}$ , where  $\dot{M}_{\text{Edd}} \equiv 10L_{\text{Edd}}/c^2$  is the Eddington accretion ratio and  $L_{\text{Edd}}$  is the Eddington luminosity) (e.g., [18–21]). The radio emission from radio-loud LLAGNs at frequencies below  $\sim 10^2$  GHz is believed to be associated with the non-thermal synchrotron contributed by their jet. At different observational frequencies, the surface where the jet non-thermal synchrotron emission transits from optically thin ( $\tau < 1$ , where  $\tau$  is the optical depth) to optically thick ( $\tau > 1$ ) is responsible for the observed “core shift” (e.g., [22,23]); the shift in positions of the unresolved optically thick core ( $\tau \sim 1$ ) [24].

The details of jet structure and physics can be constrained by the combination of the observed spectra and morphologies. The latter requires enough resolution for the

target source. Recently, with an angular resolution  $\sim 20 \mu\text{as}$  at 230 GHz, successful VLBI observations of black hole shadows have been achieved by the Event Horizon Telescope (EHT) collaboration [11,12,25–36]. Several jet sources have also been observed with such unprecedented resolution [37,38]. With expected improved VLBI resolutions in the future (e.g., [39]), an increasing number of black hole candidates will be resolved [40]. To this end, in this review, we focus on the current progress in modeling radio images of nearby LLAGN jets at VLBI scales, from  $\lesssim$ milliparsec scales, where the jet is launched (in the vicinity of the black hole), to the sub-parsec scales, where the jet is being accelerated and collimated. Example LLAGN sources are presented in Table 1.

There are two major components for modeling the radio image of a jet: (1) jet model and (2) radiative transfer. The jet model provides the collective details of the configuration of large-scale magnetic field lines and how plasma streams along different large-scale magnetic fields. The radiative transfer modeling is related to the photon path, the energy shift between the reference frames, and the detailed energy distribution of electrons, while the last should be constrained or motivated by observed spectra.

Depending on the scales of interest, the above-mentioned components in modeling LLAGN jets may be simplified by different assumptions. For example, near horizon scales' general relativistic effects are essential for including the gravity effect as a function of black hole spin. At scales far away from the central black hole where the gravity effect can be ignored, only special relativistic effects remain important.

This article is organized as follows. In Section 2, based on previous works of GRMHD simulations, we introduce the GRMHD paradigm for LLAGN jet formation in black hole accretion jet systems. In Section 3, the construction of a jet model is reviewed. In Section 4, important considerations in the procedure of radiative transfer are given. Model jet image features are demonstrated and discussed with a set of illustrative models. Finally, the summary and outlook will be given in Section 5.

**Table 1.** Selected example LLAGN sources with jet emission.

	$M_{\text{BH}}$ ( $10^8 M_{\odot}$ )	D (Mpc)	BH Shadow Size * ( $\mu\text{as}$ )	Accretion Rate ( $\dot{M}/\dot{M}_{\text{Edd}}$ )
M87	65 [11,12]	16.8 [11,12]	38.2	$\sim 10^{-5}$ [28]
IC 1459	11 [41]	29.2 [42]	3.72	$\sim 10^{-3}$ [43] <sup>†</sup>
Centaurus A	0.55 [44]	3.8 [45]	1.43	$\sim 10^{-5}$ [44]
3C 84	9 [46]	76.9 [46]	1.15	$\sim 10^{-2}$ [47]
Cygnus A	25 [42]	232 [42]	1.06	$\sim 10^{-2}$ [43] <sup>†</sup>
NGC 1052	1.54 [48]	20.7 [48]	0.73	$\sim 10^{-2}$ [43] <sup>†</sup>
NGC 6251	5.9 [42]	104.6 [42]	0.56	$\sim 10^{-2}$ [43] <sup>†</sup>

Notes. \* the size of black shadow is estimated by  $10 R_g$  (e.g., [49]). <sup>†</sup> the accretion rates are estimated by fitting the spectra of the sources with the RIAF model spectra [43], based on the semi-analytical RIAF model [18].

## 2. GRMHD Paradigm of Jet Formation for LLAGN

The accretion flows around LLAGNs are believed to be of the RIAF type. For a RIAF, the ion temperature ( $T_i \sim 10^{12}$  K) is much higher than electron temperatures ( $T_e \sim 10^{10-11}$  K) due to the inefficient Coulomb interaction between the ions and electrons at low accretion rates (e.g., [21,50,51]). In turn, the heat stored in the accretion flow results in a puffed-up, thick geometry of the flow.

With the rapid progress of GRMHD simulations since  $\sim 2000$  (e.g., [52–67]), details of a geometrically thick, negligible radiation feedback flow environment (such as LLAGN) have been revealed. An example GRMHD simulation result is shown in Figure 1. While large-scale magnetic field lines threaded onto the accretion flow are absent [53], large-scale magnetic field threaded onto the black hole event horizon is naturally developed in the funnel region along with the black hole's rotational axis. In such a funnel region, GRMHD extraction of black hole rotational energy along the large-scale magnetic fields can take

place, and the jet is launched at the expense of black hole energy. In fact, relativistic jets powered by the rotation of a black hole via a large-scale magnetic field attached to the event horizon are common scenes in GRMHD simulations (e.g., [68,69]).

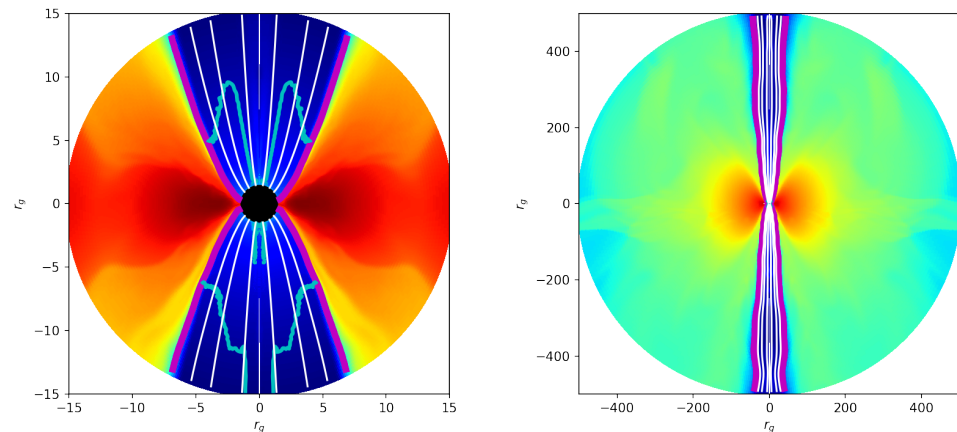


**Figure 1.** Examples of magnetic field configuration from a 2D GRMHD simulation for accretion flow with negligible radiation feedback, with small (left panel) and large (right panel) fields of view. The black hole rotational axis is aligned with that of the accretion flow. Black hole-threaded, ordered, large-scale magnetic fields (indicated as white lines) are developed along the black hole rotational axis, enclosed by the contours of  $\sigma \equiv B^2 / \rho c^2 = 1$  (purple lines). Magnetic field configurations in the region where  $\sigma < 1$  are not shown. The contours for  $u^r = 0$  (a radial component of the fluid's four velocities) are shown as cyan lines. Relativistic jets are launched from the funnel region at the expense of the rotational energy of black holes. The color shows the density on a logarithmic scale, with blue and red representing small and large densities, respectively.

The stationary GRMHD extraction process under ideal MHD conditions [70] can be viewed as an extension of the electromagnetic extraction process under force-free conditions, known as the Blandford–Znajek process [71]. The electromagnetic part is responsible for extracting the rotational energy from the rotating black hole. Therefore, efficient extraction is performed by a Poynting-dominated GRMHD flow (see also Section 3.1 for a discussion of the fluid and electromagnetic part of the GRMHD flow).

An important feature of the above-mentioned GRMHD paradigm for jet formation is the existence of the boundary for GRMHD flows streaming inward or outward along the same field line as the result of the competition of magneto-centrifugal force and gravity force acting on the plasma [70]. Such a boundary, usually called the *stagnation surface* or *separation surface* is shown as the cyan lines in Figure 1. In the *inflow* region, the GRMHD extraction process mentioned above takes place; in the *outflow* region, the flow is accelerated as a result of the conversion from electromagnetic energy to fluid energy of the GRMHD flow (e.g., [58,72]). The maximum possible jet velocity is obtained when all the electromagnetic energy converts to the fluid's kinetic energy (e.g., [73]). For both the inflow and outflow regions, starting from negligible poloidal velocities, the accelerated GRMHD flow will pass several characteristic surfaces where the poloidal fluid velocities equal the slow-magnetosonic, Alfvén, and fast-magnetosonic speed [58,70,74–76].

The launching at the expense of black hole energy implies the relationship between jet power and the efficiency of extraction, which depends on black hole spin and magnetic field strength. GRMHD simulation has demonstrated that the jet power can be larger than the accretion power with strong enough magnetic fields [66]. As the magnetic field is supported by the accretion flow environment, there exists an upper limit for possible magnetic field strength, over which the magnetic field cannot be confined by the accretion flow. Accretion flow close to such limit is conventionally referred to as MAD (Magnetically Arrested Disk) [77–80] and otherwise referred to as SANE (Standard And Normal Evolution) (e.g., [81,82]). Detailed GRMHD simulation and image modelings have

been extensively studied for the two target sources of EHT observation, M87 and Sgr A\* (e.g., [28,30,35,83–91]). In our following discussions, we do not further distinguish the jet emission features between SANE and MAD because the emission features are related to both the jet structure and assumed emission details, as will be discussed later.

### 3. Constructing Jet Model

In this section, we present an overview of constructing global jet structures and dynamics and a collection of flow properties along different large-scale magnetic field lines. As large-scale magnetic field lines are developed only in the funnel (see Figure 1), here we consider only large-scale magnetic field lines threaded onto the event horizon as the field configuration of the jet. A schematic magnetic configuration of a jet model is shown in Figure 2.

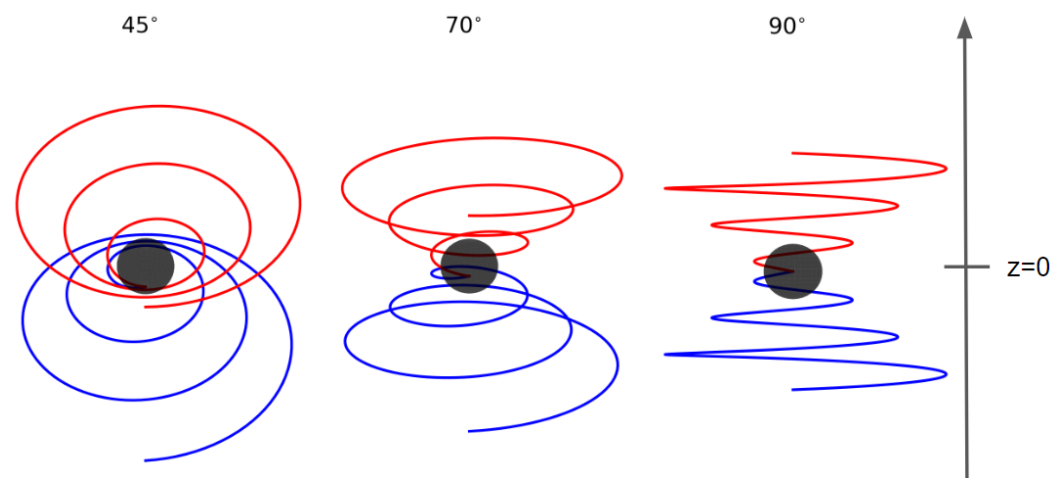


**Figure 2.** Schematic magnetic configuration of a jet model. Along the black hole rotational axis, the region above (or below) the equatorial plane is referred to as  $z > 0$  (or  $z < 0$ ). Cases for different viewing angles with respect to the rotational axis are shown (from left to right:  $45^\circ$ ,  $70^\circ$ , and  $90^\circ$ ).

#### 3.1. Semi-Analytical Jet Models

Semi-analytical jet models are usually assumed to be axisymmetric and stationary. MHD flow streaming in a magnetosphere consists of an ordered, large-scale magnetic field; it is convenient to decompose the equation of motion for MHD flow along the trans-field direction and parallel-field direction, which results in the so-called Grad–Shafranov equation (GSE) and wind equation (or the Bernoulli equation) (e.g., [92]). The solution to GSE corresponds to the magnetic field configuration, and the solution to the wind equation corresponds to the flow acceleration along the field.

While solving the GSE is a challenging task (e.g., [93–95]), a common working proposal to describe the global magnetic field geometry of a black hole jet is simple: applying the approximated solution for a force-free magnetic field [61,65]

$$\Psi = r^\nu (1 - \cos \theta), \quad (1)$$

where  $0 \leq \nu \leq 1.25$  controls the geometry ( $\nu = 0$ : split-monopole-like configuration;  $\nu = 1$ : parabolic field line). With such a stream function, different poloidal magnetic field lines are determined by the contours of  $\Psi = \text{constant}$ . Even for an MHD jet, we can expect that the configuration described by the force-free solution, such as Equation (1), remains good given that the flow is Poynting dominated. By measuring the jet width, the observed jet collimation for M87 is consistent with  $\nu = 0.75$  [96–98].

Before we move onto the MHD jet models, it is illustrative to estimate the jet dynamics with the drift velocity under the force-free assumption (see [99] for the details of the model, and also [61,100] for the detailed analysis of the acceleration properties). Without

consideration of the plasma effect, the velocity is determined solely by the assumed angular velocity of the field and the field configuration. In addition, with a prescribed poloidal magnetic field, the toroidal component of the magnetic field can be estimated under force-free assumption far from the jet [99]:

$$B^\phi = \frac{-2\Psi\Omega_F}{R} \quad (2)$$

where  $R$  is the cylindrical radius and  $\Omega_F(\Psi)$  (a conserved quantity along the field line  $\Psi$ ) is the angular velocity of the magnetic field. An overview of the magnetic configuration and velocity of the force-free jet model is given in Table 2. Note that  $B^r$  and  $B^\phi$  change signs above and below the equatorial plane, while  $B^\theta$  retains the same sign (also see Figure 2). Along the field line, the continuity equation requires the number density  $n$  as follows

$$\frac{n}{B^2} = \text{constant} , \quad (3)$$

where  $B$  is the strength of the magnetic field [99].

**Table 2.** Overview of the structure of a force-free jet model <sup>†</sup>.

	$z > 0$	$z < 0$
$B^r$	$>0$	$<0$
$B^\theta$	$<0$	$<0$
$B^\phi$	$<0$	$>0$
$v^r \propto -B^r B^\phi$	$>0$	$>0$
$v^\theta \propto -B^\theta B^\phi$	$<0$	$>0$
$v^\phi \propto (B_r^2 + B_\theta^2)$	$>0$	$>0$

Notes. <sup>†</sup> region  $z > 0$  and  $z < 0$  can be referred to in Figure 2.

As the gravity effect is ignored, the velocity in the force-free jet model is always outward. The near horizon features suggested by the GRMHD framework (such as the existence of the stagnation surface and the inflow region) are, therefore, absent. Nevertheless, by applying a distance floor under which the emission near the horizon is excluded, the covariant form of the force-free jet model provides helpful insights on horizon-scale emission features (e.g., [99,101–103]). It is worth noting that the predicted velocity of a force-free jet seems too large compared to the observed values (e.g., [10,98]). By reducing the toroidal magnetic component (to mimic the effect due to mass loading of magnetic fields), further modification of the force-free jet with a reasonable terminal Lorentz factor is considered in [101]. For practical applications to scales much larger than black hole size, the vector form of the force-free jet model can be applied [104,105].

Under the ideal MHD condition, there are four conserved quantities for an axisymmetric, stationary, cold (i.e., the pressure of the flow is ignored) GRMHD flow: the angular velocity of the magnetic field  $\Omega_F$ , the mass loading (particle number flux per unit electromagnetic flux; see also Equation (6)), the total energy  $E$ , and the angular momentum  $L$  of the flow. The flow velocity can be obtained by solving the wind equation (along a field line  $\Psi$ ), which has the form

$$u_p^2 + 1 = \left(\frac{E}{\mu}\right)^2 \mathcal{U}(r, \theta; \Psi) , \quad (4)$$

where  $u_p^2 = u^r u_r + u^\theta u_\theta$ ,  $\mu$  is the relativistic enthalpy, and  $\mathcal{U}$  is related to the conserved quantities and the assumed background spacetime [70,106–111].

As an interesting feature of the solution to the wind equation, only the correct combination of the four conserved quantities can provide physical flow, which can successfully pass the fast magnetosonic point and reach infinity [70,72,112]). In addition, the toroidal field can not be prescribed as a prior but need to be obtained from the solution of the wind equa-

tion. Furthermore, for Poynting-flux-dominated flow, the plasma loading onto a large-scale force-free magnetic field line can perturb the field configuration during its MHD acceleration (e.g., [113,114]). All these have made the construction of a semi-analytical GRMHD jet model challenging. By analysis of the wind equation, sophisticated relationships between the covariant components of toroidal and poloidal magnetic field [74,115]

$$\frac{B_\phi}{B_p} = \mathcal{B}(r; \Psi) \quad (5)$$

have been found to guarantee physical, trans-fast magnetosonic MHD outflow solutions. An increase in the ratio can lead to a lower terminal velocity [74,75]. Based on the relationships, a semi-analytical GRMHD jet model for collective flow properties have been recently constructed [75,116]. Further away from the central black hole (where gravitational effect is not essential), GRMHD jet solutions are in good agreement with relativistic MHD solutions [75].

An overview of the GRMHD flow properties for both inflow ( $u^r < 0$ , the radial component of the four-velocity of the flow) and outflow ( $u^r > 0$ ) regions is presented in Table 3. As shown in the table, in the inflow region ( $u^r < 0$ , the radial component of the four-velocity of the flow), a successful extraction and positive outward energy flux  $\mathcal{E}^r = Eu^r > 0$  is possible only when  $E < 0$ , and, therefore, only for Poynting-flux-dominated GRMHD inflow ( $E_{EM} \gg E_{FL}$ , the subscripts EM and FL correspond to the electromagnetic part and the fluid part of the GRMHD flow). A continuous propagation of the positive outward energy flux can be applied to match the inflow and outflow solutions [72]. Required by the continuity equation, written in a way similar to Equation (3), the number density  $n$  follows

$$\frac{nu^p}{B^p} = \text{constant}, \quad (6)$$

where superscript  $p$  represents the poloidal component.

### 3.2. GRMHD Simulation Models

The definition of the jet for GRMHD simulations varies with different studies and motivations. The boundary between the jet and the accretion flow may be defined by the ratio between magnetic energy and fluid rest energy ( $\sigma = B^2/\rho c^2$ , where  $B$  is the field strength and  $\rho$  is the density), the Bernoulli parameter ( $B_e = -hu_t$ , where  $h$  is the relativistic enthalpy and  $u_t$  is the  $t$ -component of the four velocities of the fluid), or even the angle (see [117] for comparisons of some of these definitions). Among the above possible choices, here we refer to the  $\sigma \geq 1$  region as the jet region in GRMHD numerical simulations because the large-scale field lines are enclosed within the region  $\sigma > 1$  (see also Figure 1). Note that the  $\sigma = 1$  contours attach to the event horizon. In comparison, in the region where  $\sigma < 1$ , the magnetic field contours reveals chaotic magnetic configurations in the accretion flow, as a result of magneto-rotational instability (MRI) [118].

Complementarily to the semi-analytical approach, the numerical simulation may suffer from the numerical dissipate process. To prevent the density from being too low in the computational domain (usually within the domain  $r < 10 R_g$  and  $\sigma > 1$ ) and from crashing the numerical simulation, an artificial density threshold is applied (e.g., [58,119]).

**Table 3.** Poynting-flux-dominated GRMHD flow properties along large-scale magnetic field threading black hole<sup>†</sup>. The table is modified from [72].

	$z > 0$		$z < 0$	
	Inflow	Outflow	Inflow	Outflow
$u^r$	<0	>0	<0	>0
$u^\theta$	>0	<0	<0	>0
$u^\phi$	>0	>0	>0	>0
$u^t$	>0	>0	>0	>0
$E = E_{\text{FL}} + E_{\text{EM}}$	<0	>0	<0	>0
$E_{\text{FL}}$	>0	>0	>0	>0
$E_{\text{EM}}$	<0	>0	<0	>0
$L = L_{\text{FL}} + L_{\text{EM}}$	<0	>0	<0	>0
$L_{\text{FL}}$	>0	>0	>0	>0
$L_{\text{EM}}$	<0	>0	<0	>0
$\mathcal{E}^r = \mathcal{E}_{\text{FL}}^r + \mathcal{E}_{\text{EM}}^r$	>0	>0	>0	>0
$\mathcal{E}_{\text{FL}}^r$	<0	>0	<0	>0
$\mathcal{E}_{\text{EM}}^r$	>0	>0	>0	>0

Notes. <sup>†</sup> In the table, all subscript FL and EMs correspond to the fluid part and the electromagnetic part of the GRMHD flow, respectively. For a Poynting-flux-dominated flow,  $E_{\text{EM}} > E_{\text{FL}}$ . Region  $z > 0$  and  $z < 0$  can be referred to in Figure 2.

In principle, GRMHD simulations can provide sophisticated modeling, including both jet and the circum-jet environment, as well as their dynamical features. Large-scale simulations with a computation domain, e.g.,  $\gtrsim 10^4 R_g$ , can be relatively expensive (especially for 3D simulations) as a longer computational time is required to reach a stationary and meaningful physical state of the system.

### 3.3. General Features

For GRMHD flow along large-scale fields, there are two light surfaces respectively in the inflow and outflow region. Here we are interested in the light surface for the outflow, which provides an important reference for the structure and dynamics of the jet. In flat spacetime, the outer light surface has a cylinder profile (if  $\Omega_F$  is constant across field lines), with the cylindrical radius  $R_L = c/\Omega_F$ . Beyond the light cylinder, the poloidal flow velocity must be larger than the toroidal velocity, as shown in Figure 3. For a Poynting-flux-dominated MHD flow, the Alfvén surface almost coincides with the light cylinder, implying that the toroidal magnetic field becomes larger than the poloidal field outside the light cylinder.

Noting that the location of the light cylinder is related to  $\Omega_F$ , the jet properties as a function of black hole spin can be understood by how  $\Omega_F = \alpha\Omega_H$  is associated with the black hole angular velocity  $\Omega_H$ , where  $\alpha \lesssim 0.5$  is usually considered (e.g., [58,71]). The horizon scale properties, such as the black hole spin, are then related to the large-scale jet properties through the jet boundary and the angular velocity of the large-scale magnetic field lines. For semi-analytical models, the jet boundary can be defined by the last large-scale magnetic field line that is attached to the event horizon at the equatorial plane. For GRMHD simulation models, the jet boundary can instead be defined by the  $\sigma = 1$  contour (see Figure 1).

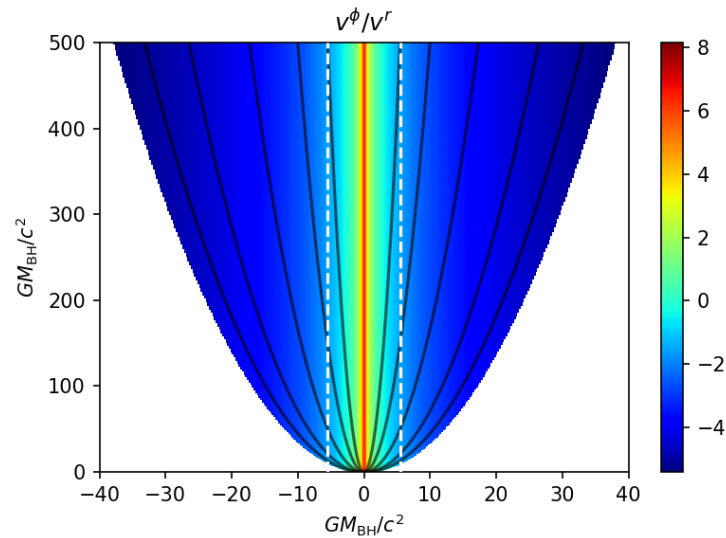


**Figure 3.** Ratio between the toroidal velocity  $v^\phi = u^\phi / u^t$  and radial velocity  $v^r = u^r / u^t$  of a force-free jet, as computed semi-analytically from the 4-velocity  $u^\alpha$  of the covariant force-free jet model with black hole spin  $a = 0.9$ . The field line geometry is  $\nu = 1$  (Equation (1)), and the angular velocity of all the field lines is half of the angular velocity of the hole. Located within the light cylinders (whose distance to the black hole rotational axis can be approximated by the location where  $R_L = c/\Omega_F$ , as shown by the white vertical dashed lines), the toroidal velocity-dominated regions ( $v_\phi/v_r > 1$ ) are shown in red. Representative field lines are shown with black lines. The boundary of the jet region is defined by the last field line, which is attached to the event horizon at the equatorial plane. Note that the radial velocity is positive in all regions as the gravity effect is not included in the model.

#### 4. Modeling Jet Emission

Synchrotron radiation is responsible for the observed radio emission from relativistic jets. The unpolarized and polarized emissivity and absorption coefficients of synchrotron radiation from different electron energy distribution have been extensively studied (e.g., [120–122]). The coefficients, in general, depend on the electron number density, the local magnetic field strength, and parameters that characterize the energy distribution. For example, for an ensemble of electrons, relativistic Maxwellian energy distribution is associated with the electron temperature, and power-law energy distribution is associated with the power-law index and minimum and maximum particle electrons. A hybrid distribution (thermal plus power-law) is of interest to reflect a more realistic energy distribution. In a hybrid case, the source function  $S_\nu$  for the radiative transfer is constructed by the sum of the contributed emissivity coefficients  $j_\nu$  and absorption coefficients  $\alpha_\nu$  (e.g., [123]):  $S_\nu = (\sum_i j_\nu^i) / (\sum_i \alpha_\nu^i)$ . Recently, the kappa distribution, which smoothly connects the thermal core to a power-law tail, has also been considered (e.g., [88–90,124]).

Due to the relativistic speed of the jet and the strong gravity in the vicinity of the black hole, the energy shift between the comoving frame and the observer's frame requires additional care in the radiative transfer computation. The covariant form for the energy shift (e.g., [125,126]) is

$$\frac{v_\infty}{v_{\text{local}}} = \frac{(g_{\alpha\beta} p^\alpha u^\beta)|_\infty}{(g_{\alpha\beta} p^\alpha u^\beta)|_{\text{local}}}, \quad (7)$$

where  $g_{\alpha\beta}$  is the background spacetime metric,  $p^\alpha$  is the four-momentum of the photon, and  $u^\alpha$  is the four-velocity of the fluid,  $u^\alpha|_{\text{local}}$ , or the distant observer,  $u^\alpha|_\infty = (1, 0, 0, 0)$ . The background spacetime would affect the  $g_{\alpha\beta}$  term in the above equation and also the geodesics. A number of general relativistic radiative transfer (GRRT) tools (e.g., see [127] and the references therein) have been developed to take care of the radiative transfer computation in curved spacetime by solving its Lorentz invariant form (e.g., [126]). When the scattering effect is not crucial, the observed flux of the received ray can be integrated

along the geodesics backward in time. In flat spacetime ( $g_{\alpha\beta} = \eta_{\mu\nu}$ , the Minkowski metric), the photon geodesic is simply a straight line, and Equation (7) reduces to the familiar relativistic Doppler effect characterized by the Doppler factor  $\mathcal{D}$  (e.g., [24]):

$$\frac{v_{\infty}}{v_{\text{local}}} = \mathcal{D} = \Gamma^{-1}(1 - \beta \cos\theta)^{-1}, \quad (8)$$

where  $\Gamma$  is the Lorentz factor of the jet,  $\beta = v/c$ , and  $\theta$  is the angle between the jet and the observer.

The origin of non-thermal electrons responsible for the jet emission remains a subject of considerable debate. There are different approaches to model the jet emission, with different assumptions of electron energy distribution and spatial distribution. In fact, the injection of non-thermal electrons can rely on the microscope process and is outside the scope of the simulated parameters themselves. If it is the case, we may treat the non-thermal electron as a free parameter. Following such a philosophy, the electron number density does not need to satisfy the relationship derived from the continuity equation, Equations (3) and (6). A possible approach is to link the internal energy of the non-thermal electrons to the magnetic field energy with a fraction  $\eta$  and a possible modification function  $\mathcal{F}$  [117,128] (see also [129] for further considerations)

$$u_{\text{nth}} = \eta \frac{B^2}{8\pi} \mathcal{F}. \quad (9)$$

Interestingly, if the brightness temperature of the observed source is comparable to or smaller than the theoretical possible electron temperature, thermal synchrotron is also capable of being responsible for the observed emission (e.g., [28,35]). From a modeling point of view, thermal synchrotron emissions may originate from regions outside the funnel where large-scale magnetic field configuration appears. A funnel wall can be defined by the region between the funnel and the corona of the flow [59]. In one-fluid GRMHD simulations, only the species (i.e., ions) that dominate the dynamics are simulated. Therefore, the ratio  $\mathcal{R}$  between  $T_i$  and  $T_e$  can be treated as a free parameter:

$$\frac{T_i}{T_e} = \mathcal{R} \geq 1. \quad (10)$$

While  $\mathcal{R}$  is related to microscopic electron thermodynamics, the phenomenological relationship of  $\mathcal{R}$  can be constructed with  $\sigma$  and plasma beta  $\beta_P = P_{\text{gas}}/P_{\text{mag}}$ , defined by the ratio between the gas pressure and magnetic pressure. The electron thermodynamics are included in more sophisticated GRMHD simulations (see Section 5).

In the following, we consider four illustrative models. The models are constructed by combining the above considerations, and their properties are summarized in Table 4. As the synchrotron radiation becomes more optically thin at higher frequencies, low frequency observations are capable of observing the downstream, extended jet emission. We first demonstrate the modeling of sub-parsec scale jet emissions at relatively lower frequencies (43 and 86 GHz), then milliparsec jet emissions at a higher frequency (230 GHz), assuming that the mass of the central black hole is  $5 \times 10^9 M_{\odot}$  and the distance to the black hole is 10 Mpc ( $1 R_g \sim 4.9 \mu\text{as}$  for reference). With a black hole spin of  $a = 0.9$ , the viewing angle to the jet axis is assumed to be  $135^\circ$ , and, therefore, the black hole spin vector is pointing away from the observer. The black hole mass, distance, and viewing angle are similar to the parameters for M87.

For the semi-analytical model, the covariant force-free jet model is applied. To mimic the funnel shape of the GMRHD jet model, the jet geometry  $\nu = 1$  is applied in Figure 3. The dynamics of the force-free model can be referred to in Figure 3. For GRMHD jet models, the numerical simulation data are from a 2D GRMHD simulation (as shown in Figure 1) performed by the public GRMHD code HARM [130,131], with initial and boundary conditions

similar to the setup in [98] but with a larger magnetic flux reservoir. The post-processing for radiative transfer is performed by the public GRRT code *Odyssey* [132].

**Table 4.** Overview of Illustrative Models \*.

Jet Model	Emission		
	Thermal Synchrotron	Non-Thermal Synchrotron	* Applying Floor
semi-analytical force-free jet model (with floor)		✓	✓
GRMHD simulation jet model A		‡✓	
GRMHD simulation jet model A (with floor)		‡✓	✓
GRMHD simulation jet model B	†✓		

Notes. \*  $M_{\text{BH}} = 5 \times 10^9 M_{\odot}$ ,  $a = 0.9$ ,  $D = 10$  Mpc ( $1 R_g \sim 4.9 \mu\text{as}$ ), and viewing angle  $i = 135^\circ$ . \* ignore all emissions from jet regions below the distance floor  $z = r \sin \theta < 10R_g$ . ‡ only from region  $\sigma = b^2/\rho c^2 > 1$  in the simulation data. † only from region  $\sigma < 1$  in the simulation data.

#### 4.1. Modeling Black Hole Jets at Sub-Parsec Scales

The 43 and 86 GHz model images for the GRMHD jet model A (non-thermal synchrotron from the region  $\sigma > 1$ ) and model B (thermal synchrotron from the region  $\sigma < 1$ ) are shown in Figure 4 on a logarithmic scale. The projected black hole spin axis is pointing to the left, and the forward jet is pointing to the right. For both of the models, the electron number density is normalized so that the total flux in the same field of view ( $500R_g \times 500R_g$ ) is  $\sim 0.4$  Jy at 43 GHz.

For all jet model images, the imprints of jet dynamics are shown: the forward jet is brighter than the counter jet, and the incoming (bottom) side of the jet is brighter than the receding (top) side. For each model, the 86 GHz image is less extended compared to the 43 GHz image, as the jet becomes more transparent. Such a feature is associated with the observed shift in the position of the unresolved VLBI core (i.e., core shift) of jetted radio sources.

With those common features, the resulting jet model images are related to the emission details considered in the radiative transfer. Non-thermal synchrotron emissions from the funnel region ( $\sigma > 1$ ) are computed for GRMHD jet model A. Adopting  $\eta = 0.1$  and  $\mathcal{F} = 1$  in Equation (9) (same assumption in [117]), the number density of non-thermal electrons can be determined by [117]:

$$n_{\text{nth}} = \eta \frac{B^2}{8\pi} \frac{p-2}{p-1} (m_e c^2 \gamma_{\text{min}})^{-1} \quad (11)$$

where  $p = 3.5$  is the power law index of the electron energy distribution between the low-energy cutoff ( $\gamma_{\text{min}} = 50$ ) and the high-energy cutoff. Under the assumption, the electron number density is solely determined by the magnetic field strength  $B$  of the jet (and independent of the number density given from the simulation data).

GRMHD jet model B shows thermal synchrotron emission outside the jet funnel (regions where  $\sigma < 1$ ). The number density of thermal electrons is considered by scaling its numerical value to fit the total target flux ( $\sim 0.4$  Jy at 43 GHz), with the ratio  $\mathcal{R}$  in Equation (10) following the physically motivated relationship with  $\beta_p$  [133],

$$\mathcal{R} = \mathcal{R}_{\text{high}} \left( \frac{\beta_p^2}{1 + \beta_p^2} \right) + \mathcal{R}_{\text{low}} \left( \frac{1}{1 + \beta_p^2} \right), \quad (12)$$

with  $\mathcal{R} \sim \mathcal{R}_{\text{high}} = 80$  at high  $\beta_p$  regions (preferentially in the main flow body near the equatorial plane) and with  $\mathcal{R} \sim \mathcal{R}_{\text{low}} = 1$  at low  $\beta_p$  regions (preferentially near the jet funnel region). The limb-brightening feature observed for M87 (e.g., [9] can be reproduced with this approach by enhancing the  $\mathcal{R}_{\text{high}}$  value [133]. Other post-processing options for

thermal synchrotron jet emissions have been applied in previous studies. For example, one can assume a constant  $T_e$  (isothermal jet) [83,84], or constant  $\mathcal{R}$  (constant ratio jet) [84] in the region where  $\beta_P < \beta_{cut} \sim 0.2$ , with or without an excised  $\sigma < \sigma_{cut}$  region. Applying constant  $\mathcal{R}$  for all (both jet and accretion) regions has also been considered in [62,85]. In addition, hybrid synchrotron emissions with a kappa distribution (kappa jet) are also possible considerations [88–90,124].

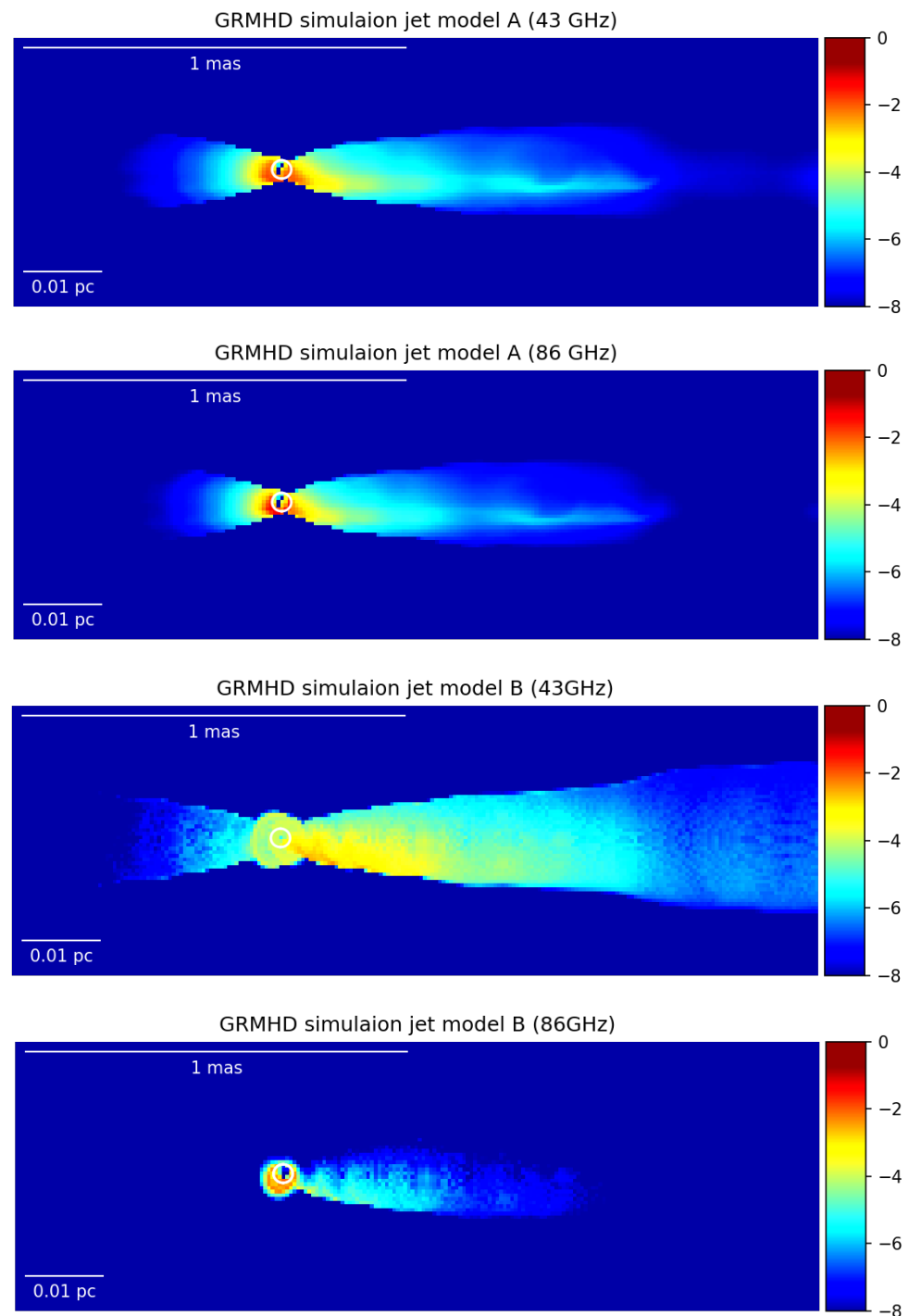


**Figure 4.** Model synchrotron images at 43 and 86 GHz for GRMHD jet models A and B. The projected black hole axis is pointing to the right. The images are shown on a logarithmic scale. For reference, the size of the black hole shadow is indicated by the white circle near the jet base. The color bar indicates Jy/pixel.

As all the emissions within  $\sigma < 1$  are included in GRMHD jet model B, the image morphology near the jet base (the regions near the white circles in the plots) has a much larger size compared to that of GRMHD jet model A. These emissions are mainly contributed by the accretion flow. Another striking jet feature between GRMHD jet models shown in Figure 4 is the relatively brighter stripe near the jet “spine” in the GRMHD jet model A images. Such a feature is also shown in the model images of the semi-analytical force-free jet model, as discussed below.

In Figures 5 and 6, a floor condition is applied to both GRMHD jet model A and the force-free jet model. The emission below a certain floor height  $z = 10 R_g$  to the black hole is excluded. The purpose is twofold. First, to avoid the emission feature from the unphysical flow dynamics in the force-free jet model. Second, to mimic the case if non-thermal electrons are injected at a certain height. The non-thermal electron number density of the force-free model (with the floor) is assigned to fit the total flux of GRMHD jet model A (with the floor) at 43 GHz. In Figures 5 and 6, the relatively brighter stripe near the “spine” in the jet is shown in both models. This is due to the jet dynamics: across the jet (vertical direction of the figures), from the jet spine to the jet boundary, the flow velocity transits from toroidal-dominated to poloidal-dominated (see also Figure 3). In between, the flow direction would be swept through the observer’s line of sight, resulting in a strong relativistic Doppler beaming effect ( $\theta \sim 0$  in Equation (8)). A similar feature has also been found in [105].

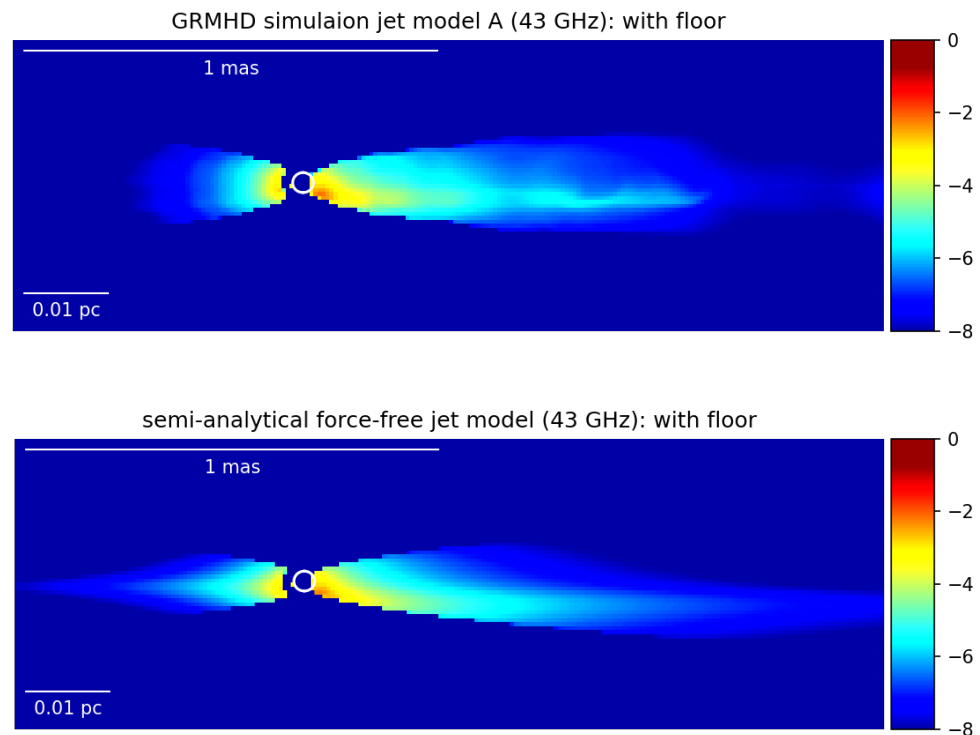


**Figure 5.** Model synchrotron images at 43 GHz for GRMHD jet model A (with floor) and force-free jet model (with floor). Emissions below floor height  $z = 10 R_g$  of the black hole are excluded.

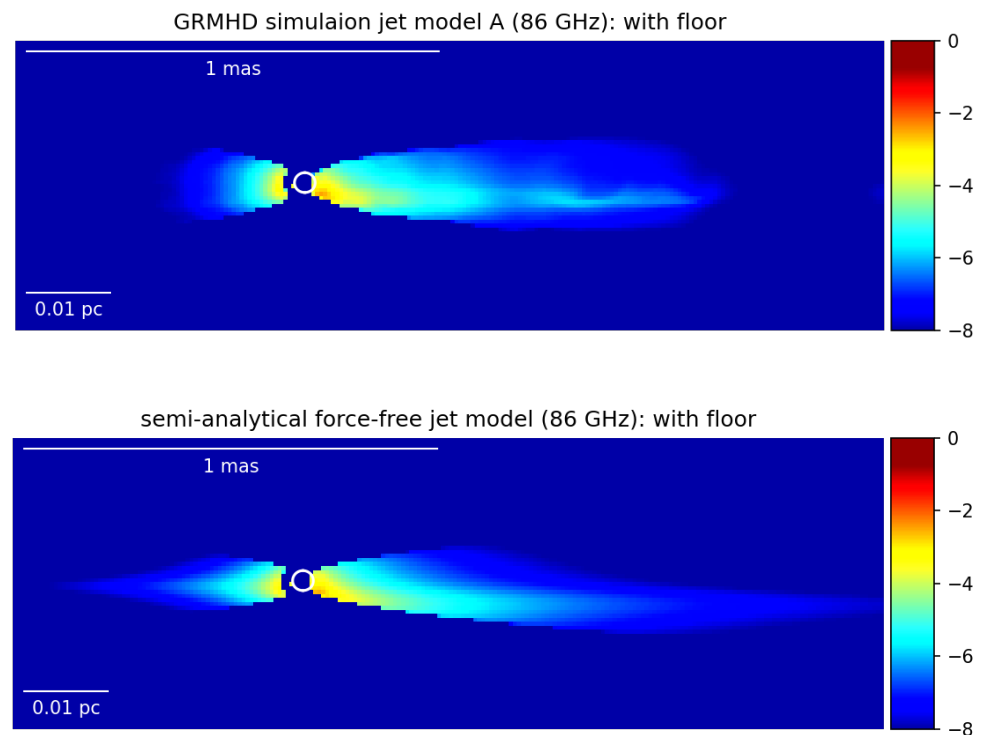


**Figure 6.** Same as Figure 5, but for 86 GHz.

#### 4.2. Modeling Black Hole Jets Close to the Jet Base

The 230 GHz model images for GRMHD jet models A and B are shown in Figure 7, with the same parameters applied to Figure 4. For our setup, at 230 GHz, the black hole shadow can be observed. As can be seen in the images, the horizon scale image is sensitive to the ratio between the contribution of accretion flow and jet.

For GRMHD jet model A, the black hole shadow (the dashed circle in the plot) is enclosed by the jet emission. Surrounding the black hole shadow, the ring-like structure with a brighter side at the bottom is actually mainly contributed by the emission of the counter jet (see also [117]). For GRMHD jet model B, in comparison, the horizon scale image further reveals the motion and emission of the accretion flow, resulting in a larger size of the emission region. For GRMHD jet model B, the black hole shadow is partially blocked by the accretion flow. The imprint of the funnel wall jet can also be seen outside the bright accretion flow emission (near the middle, at the bottom of the figure).

The models with floors are shown in Figure 8. The image morphology is similar for GRMHD jet model A with a floor and for the force-free jet model. As the injection location moves further away from the black hole, the black hole shadow image becomes less obvious. There appears a compact emission region at the incoming side of the jets, with its emission centroid being well outside the location of the black hole shadow. Such features have also been shown in [101].

As demonstrated, the horizon scale images can be largely affected by the uncertainties of emission regions and types of synchrotron radiation. Nevertheless, the background knowledge of jet dynamics and radiative transfer details can help to interpret the environment around the jet base.

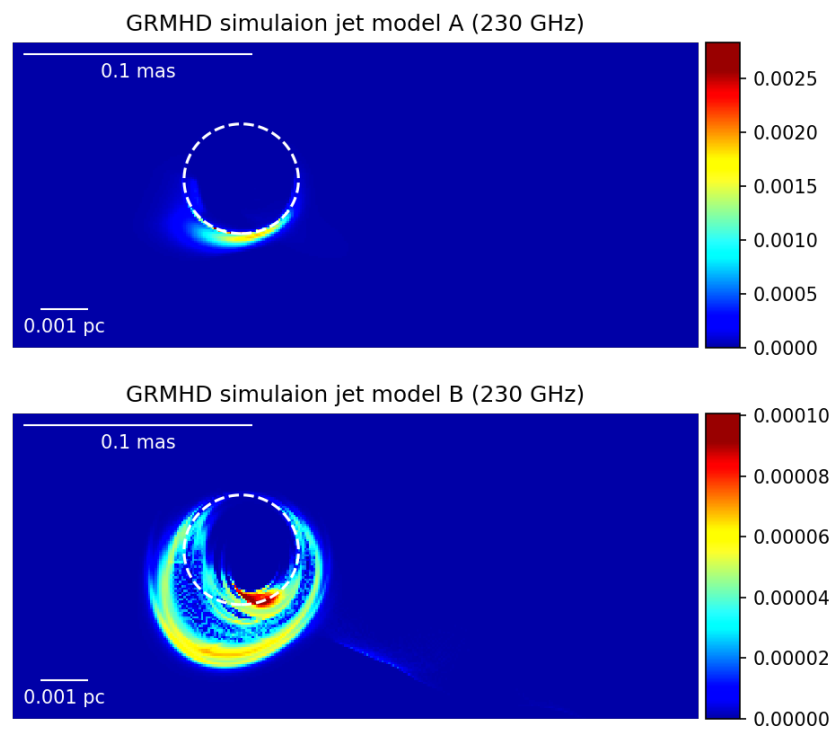


**Figure 7.** Model synchrotron images at 230 GHz for GRMHD jet models A and B. The images are shown on a linear scale. For reference, the size of the black hole shadow is indicated by the dashed white circle.

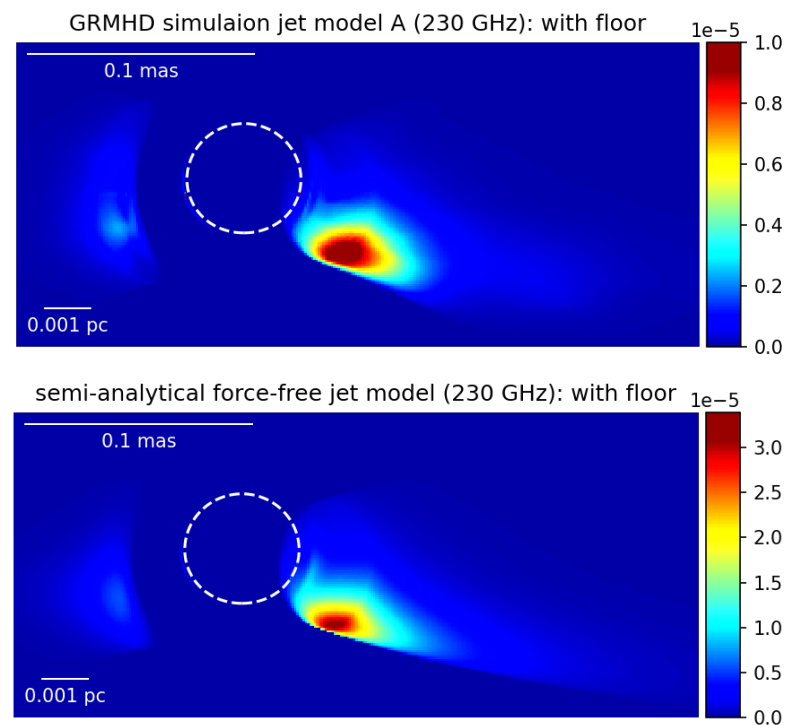


**Figure 8.** Model synchrotron images at 230 GHz for GRMHD jet model A (with the floor) and the force-free jet model (with the floor). The images are shown on a linear scale. For reference, the size of the black hole shadow is indicated by the dashed white circle.

## 5. Discussion and Outlook

The aim of the review is to summarize and discuss the current progress in modeling the rich features of LLAGN jets at VLBI scales. The modeling of jet images can be performed with jet models and emission details. Jet models can be constructed by semi-analytical approaches or from numerical simulations. The latter is a powerful tool for modeling the black hole accretion jet system, including its time-dependent features. The simulations with a large enough computational domain ( $\gtrsim 10^3 R_g$ ) can provide enough information to model jet properties across different spatial scales and frequencies and compare them with observations, e.g., spectra and core shift measurements (e.g., [76,89]), directly. The former, alternatively, provides a flexible and heuristic way of exploring jet physics and properties, given that the key physics can be properly included in the model. The emission details add different complications to the energy distribution of electrons and the emission region from the black hole accretion jet system. To explore the combined effects of the above considerations on the resulting images, jet image features at different frequencies, and different spatial scales are demonstrated with illustrative models.

As demonstrated by our illustrative models, exploring jet images down to the innermost region of the jet is important for several reasons. First, the jet image is jointly determined by the jet dynamics and mass loading. As the jet dynamics are associated with the central engine, the jet image is a possible diagnostic for the property of the central black hole and the required origin of energetic electrons [99,104,105]. Second, the ratio of the contributions between the jet and accretion flow near the sub-mm bump of LLAGN cannot be solely determined by the spectra (see, e.g., [117]) for examples). Based on the background knowledge of the emission features of jet and accretion, the observed morphology of the jetted LLAGN can provide valuable constraints to their relative importance [99,117].

Among the uncertainties in VLBI jet image modeling, electron heating microphysics or injection of non-thermal electrons are important directions to be explored [134]. Interestingly, these may link to possible correlations with other observational frequencies, e.g., X-rays [135]. Is the injection process stationary or intermittent? After injection, what are the effect of the subsequent cooling process? Does the stagnation surface play any special role in the injection [90,136–138]? All these details are expected to leave observable imprints on the resulting jet image. More advanced, state-of-the-art simulations, including electron thermodynamics, radiation, or beyond one-fluid approaches, have brought more sophisticated investigations into (part of) the above questions [86,87,91,139–143]. It is also possible to construct dynamical features onto the stationary semi-analytical jet model [103].

Although not discussed in the paper, within the VLBI scales of our interest, there are also several important topics for jet modeling. For example, the jet polarization due to circum-jet materials [128], the jets from tilted disks [144–148], jet composition [149–151], and the possible mass-loading due to mixing between the jet and surroundings [76]. More discussion of GRMHD simulation modeling of jet formation can be seen in [152]. The magnetic configuration (Figure 2) may also be revealed by polarization observations at horizon scales [153].

**Author Contributions:** H.-Y.P. wrote the draft of the paper and performed the model image computations; M.N. performed the numerical simulation. K.A. and M.N. improved the work by providing insightful comments and discussions. All authors have read and agreed to the published version of the manuscript.

**Funding:** This research was funded by Ministry of Education (MoE) Yushan Young Scholar Program, and the Ministry of Science and Technology (MOST), under the grant 110-2112-M-003-007-MY2.

**Data Availability Statement:** Not applicable.

**Acknowledgments:** We thank Wen-Ping Lo for helping with the preparation of Table 1. We thank the anonymous referees for helpful comments and suggestions.

**Conflicts of Interest:** The authors declare no conflict of interest.

## Abbreviations

The following abbreviations are used in this manuscript:

VLBI	Very-Long Baseline Interferometry
MHD	Magnetohydrodynamics
GRMHD	General Relativistic Magnetohydrodynamics
GRRT	General Relativistic Radiative Transfer
MAD	Magnetically Arrested Disk
SANE	Standard And Normal Evolution
EHT	Event Horizon Telescope
GSE	Grad–Shafranov Equation

## References

- Nagar, N.M.; Falcke, H.; Wilson, A.S.; Ulvestad, J.S. Radio sources in low-luminosity active galactic nuclei. III. “AGNs” in a distance-limited sample of “LLAGNs”. *Astron. Astrophys.* **2002**, *392*, 53–82. [[CrossRef](#)]
- Nagar, N.M.; Falcke, H.; Wilson, A.S. Radio sources in low-luminosity active galactic nuclei. IV. Radio luminosity function, importance of jet power, and radio properties of the complete Palomar sample. *Astron. Astrophys.* **2005**, *435*, 521–543. [[CrossRef](#)]
- Doeleman, S.S.; Weintroub, J.; Rogers, A.E.E.; Plambeck, R.; Freund, R.; Tilanus, R.P.J.; Friberg, P.; Ziurys, L.M.; Moran, J.M.; Corey, B.; et al. Event-horizon-scale structure in the supermassive black hole candidate at the Galactic Centre. *Nature* **2008**, *455*, 78–80. [[CrossRef](#)]
- Hada, K.; Doi, A.; Nagai, H.; Inoue, M.; Honma, M.; Giroletti, M.; Giovannini, G. Evidence for a Nuclear Radio Jet and its Structure down to  $100$  Schwarzschild Radii in the Center of the Sombrero Galaxy (M 104, NGC 4594). *Astrophys. J.* **2013**, *779*, 6. [[CrossRef](#)]
- Hada, K.; Kino, M.; Doi, A.; Nagai, H.; Honma, M.; Hagiwara, Y.; Giroletti, M.; Giovannini, G.; Kawaguchi, N. The Innermost Collimation Structure of the M87 Jet Down to  $\sim 10$  Schwarzschild Radii. *Astrophys. J.* **2013**, *775*, 70. [[CrossRef](#)]
- Mezcua, M.; Prieto, M.A. Evidence of Parsec-scale Jets in Low-luminosity Active Galactic Nuclei. *Astrophys. J.* **2014**, *787*, 62. [[CrossRef](#)]
- Hada, K.; Kino, M.; Doi, A.; Nagai, H.; Honma, M.; Akiyama, K.; Tazaki, F.; Lico, R.; Giroletti, M.; Giovannini, G.; et al. High-sensitivity 86 GHz (3.5 mm) VLBI Observations of M87: Deep Imaging of the Jet Base at a Resolution of 10 Schwarzschild Radii. *Astrophys. J.* **2016**, *817*, 131. [[CrossRef](#)]
- Boccardi, B.; Krichbaum, T.P.; Ros, E.; Zensus, J.A. Radio observations of active galactic nuclei with mm-VLBI. *Astron. Astrophys. Rev.* **2017**, *25*, 4. [[CrossRef](#)]
- Kim, J.Y.; Krichbaum, T.P.; Lu, R.S.; Ros, E.; Bach, U.; Bremer, M.; de Vicente, P.; Lindqvist, M.; Zensus, J.A. The limb-brightened jet of M87 down to the 7 Schwarzschild radii scale. *Astron. Astrophys.* **2018**, *616*, A188. [[CrossRef](#)]
- Park, J.; Hada, K.; Kino, M.; Nakamura, M.; Hodgson, J.; Ro, H.; Cui, Y.; Asada, K.; Algaba, J.C.; Sawada-Satoh, S.; et al. Kinematics of the M87 Jet in the Collimation Zone: Gradual Acceleration and Velocity Stratification. *Astrophys. J.* **2019**, *887*, 147. [[CrossRef](#)]
- Event Horizon Telescope Collaboration; Akiyama, K.; Alberdi, A.; Alef, W.; Asada, K.; Azulay, R.; Baczkowski, A.K.; Ball, D.; Baloković, M.; Barrett, J.; et al. First M87 Event Horizon Telescope Results. I. The Shadow of the Supermassive Black Hole. *Astrophys. J. Lett.* **2019**, *875*, L1. [[CrossRef](#)]
- Event Horizon Telescope Collaboration; Akiyama, K.; Alberdi, A.; Alef, W.; Asada, K.; Azulay, R.; Baczkowski, A.K.; Ball, D.; Baloković, M.; Barrett, J.; et al. First M87 Event Horizon Telescope Results. VI. The Shadow and Mass of the Central Black Hole. *Astrophys. J. Lett.* **2019**, *875*, L6. [[CrossRef](#)]
- Laing, R.A.; Bridle, A.H. Systematic properties of decelerating relativistic jets in low-luminosity radio galaxies. *Mon. Not. R. Astron. Soc.* **2014**, *437*, 3405–3441. [[CrossRef](#)]
- Potter, W.J.; Cotter, G. Synchrotron and inverse-Compton emission from blazar jets - II. An accelerating jet model with a geometry set by observations of M87. *Mon. Not. R. Astron. Soc.* **2013**, *429*, 1189–1205. [[CrossRef](#)]
- Ho, L.C. Nuclear activity in nearby galaxies. *Annu. Rev. Astron. Astrophys.* **2008**, *46*, 475–539. [[CrossRef](#)]
- Fernández-Ontiveros, J.A.; Prieto, M.A.; Acosta-Pulido, J.A.; Montes, M. The SED of Low-Luminosity AGNs at high-spatial resolution. *J. Phys. Conf. Ser.* **2012**, *372*, 012006. [[CrossRef](#)]
- Prieto, M.A.; Fernández-Ontiveros, J.A.; Markoff, S.; Espada, D.; González-Martín, O. The central parsecs of M87: Jet emission and an elusive accretion disc. *Mon. Not. R. Astron. Soc.* **2016**, *457*, 3801–3816. [[CrossRef](#)]
- Mahadevan, R. Scaling Laws for Advection-dominated Flows: Applications to Low-Luminosity Galactic Nuclei. *Astrophys. J.* **1997**, *477*, 585–601. [[CrossRef](#)]
- Ichimaru, S. Bimodal behavior of accretion disks: theory and application to Cygnus X-1 transitions. *Astrophys. J.* **1977**, *214*, 840–855. [[CrossRef](#)]
- Narayan, R.; Yi, I.; Mahadevan, R. Advection-dominated accretion model of Sagittarius A\* and other accreting black holes. *J. Astron. Astrophys. Suppl. Ser.* **1996**, *120*, 287–290.

21. Kato, S.; Fukue, J.; Mineshige, S. Black-Hole Accretion Disks: Towards a New Paradigm. 2008. Available online: <https://ui.adsabs.harvard.edu/abs/2008bhad.book.....K/abstract> (accessed on 1 October 2022).
22. Hada, K.; Doi, A.; Kino, M.; Nagai, H.; Hagiwara, Y.; Kawaguchi, N. An origin of the radio jet in M87 at the location of the central black hole. *Nature* **2011**, *477*, 185–187. [[CrossRef](#)] [[PubMed](#)]
23. Sokolovsky, K.V.; Kovalev, Y.Y.; Pushkarev, A.B.; Lobanov, A.P. A VLBA survey of the core shift effect in AGN jets. I. Evidence of dominating synchrotron opacity. *Astron. Astrophys.* **2011**, *532*, A38. [[CrossRef](#)]
24. Blandford, R.D.; Königl, A. Relativistic jets as compact radio sources. *Astrophys. J.* **1979**, *232*, 34–48. [[CrossRef](#)]
25. Event Horizon Telescope Collaboration; Akiyama, K.; Alberdi, A.; Alef, W.; Asada, K.; Azulay, R.; Baczkó, A.K.; Ball, D.; Baloković, M.; Barrett, J.; et al. First M87 Event Horizon Telescope Results. II. Array and Instrumentation. *Astrophys. J. Lett.* **2019**, *875*, L2. [[CrossRef](#)]
26. Event Horizon Telescope Collaboration; Akiyama, K.; Alberdi, A.; Alef, W.; Asada, K.; Azulay, R.; Baczkó, A.K.; Ball, D.; Baloković, M.; Barrett, J.; et al. First M87 Event Horizon Telescope Results. III. Data Processing and Calibration. *Astrophys. J. Lett.* **2019**, *875*, L3. [[CrossRef](#)]
27. Event Horizon Telescope Collaboration; Akiyama, K.; Alberdi, A.; Alef, W.; Asada, K.; Azulay, R.; Baczkó, A.K.; Ball, D.; Baloković, M.; Barrett, J.; et al. First M87 Event Horizon Telescope Results. IV. Imaging the Central Supermassive Black Hole. *Astrophys. J. Lett.* **2019**, *875*, L4. [[CrossRef](#)]
28. Event Horizon Telescope Collaboration; Akiyama, K.; Alberdi, A.; Alef, W.; Asada, K.; Azulay, R.; Baczkó, A.K.; Ball, D.; Baloković, M.; Barrett, J.; et al. First M87 Event Horizon Telescope Results. V. Physical Origin of the Asymmetric Ring. *Astrophys. J. Lett.* **2019**, *875*, L5. [[CrossRef](#)]
29. Event Horizon Telescope Collaboration; Akiyama, K.; Algaba, J.C.; Alberdi, A.; Alef, W.; Anantua, R.; Asada, K.; Azulay, R.; Baczkó, A.K.; Ball, D.; et al. First M87 Event Horizon Telescope Results. VII. Polarization of the Ring. *Astrophys. J. Lett.* **2021**, *910*, L12. [[CrossRef](#)]
30. Event Horizon Telescope Collaboration; Akiyama, K.; Algaba, J.C.; Alberdi, A.; Alef, W.; Anantua, R.; Asada, K.; Azulay, R.; Baczkó, A.K.; Ball, D.; et al. First M87 Event Horizon Telescope Results. VIII. Magnetic Field Structure near The Event Horizon. *Astrophys. J. Lett.* **2021**, *910*, L13. [[CrossRef](#)]
31. Event Horizon Telescope Collaboration; Akiyama, K.; Alberdi, A.; Alef, W.; Algaba, J.C.; Anantua, R.; Asada, K.; Azulay, R.; Bach, U.; Baczkó, A.K.; et al. First Sagittarius A\* Event Horizon Telescope Results. I. The Shadow of the Supermassive Black Hole in the Center of the Milky Way. *Astrophys. J. Lett.* **2022**, *930*, L12. [[CrossRef](#)]
32. Event Horizon Telescope Collaboration; Akiyama, K.; Alberdi, A.; Alef, W.; Algaba, J.C.; Anantua, R.; Asada, K.; Azulay, R.; Bach, U.; Baczkó, A.K.; et al. First Sagittarius A\* Event Horizon Telescope Results. II. EHT and Multiwavelength Observations, Data Processing, and Calibration. *Astrophys. J. Lett.* **2022**, *930*, L13. [[CrossRef](#)]
33. Event Horizon Telescope Collaboration; Akiyama, K.; Alberdi, A.; Alef, W.; Algaba, J.C.; Anantua, R.; Asada, K.; Azulay, R.; Bach, U.; Baczkó, A.K.; et al. First Sagittarius A\* Event Horizon Telescope Results. III. Imaging of the Galactic Center Supermassive Black Hole. *Astrophys. J. Lett.* **2022**, *930*, L14. [[CrossRef](#)]
34. Event Horizon Telescope Collaboration; Akiyama, K.; Alberdi, A.; Alef, W.; Algaba, J.C.; Anantua, R.; Asada, K.; Azulay, R.; Bach, U.; Baczkó, A.K.; et al. First Sagittarius A\* Event Horizon Telescope Results. IV. Variability, Morphology, and Black Hole Mass. *Astrophys. J. Lett.* **2022**, *930*, L15. [[CrossRef](#)]
35. Event Horizon Telescope Collaboration; Akiyama, K.; Alberdi, A.; Alef, W.; Algaba, J.C.; Anantua, R.; Asada, K.; Azulay, R.; Bach, U.; Baczkó, A.K.; et al. First Sagittarius A\* Event Horizon Telescope Results. V. Testing Astrophysical Models of the Galactic Center Black Hole. *Astrophys. J. Lett.* **2022**, *930*, L16. [[CrossRef](#)]
36. Event Horizon Telescope Collaboration; Akiyama, K.; Alberdi, A.; Alef, W.; Algaba, J.C.; Anantua, R.; Asada, K.; Azulay, R.; Bach, U.; Baczkó, A.K.; et al. First Sagittarius A\* Event Horizon Telescope Results. VI. Testing the Black Hole Metric. *Astrophys. J. Lett.* **2022**, *930*, L17. [[CrossRef](#)]
37. Kim, J.Y.; Krichbaum, T.P.; Broderick, A.E.; Wielgus, M.; Blackburn, L.; Gómez, J.L.; Johnson, M.D.; Bouman, K.L.; Chael, A.; Akiyama, K.; et al. Event Horizon Telescope imaging of the archetypal blazar 3C 279 at an extreme 20 microarcsecond resolution. *Astron. Astrophys.* **2020**, *640*, A69. [[CrossRef](#)]
38. Issaoun, S.; Wielgus, M.; Jorstad, S.; Krichbaum, T.P.; Blackburn, L.; Janssen, M.; Chan, C.k.; Pesce, D.W.; Gómez, J.L.; Akiyama, K.; et al. Resolving the Inner Parsec of the Blazar J1924-2914 with the Event Horizon Telescope. *Astrophys. J.* **2022**, *934*, 145. [[CrossRef](#)]
39. Doeleman, S.; Blackburn, L.; Dexter, J.; Gomez, J.L.; Johnson, M.D.; Palumbo, D.C.; Weintraub, J.; Farah, J.R.; Fish, V.; Loinard, L.; et al. Studying Black Holes on Horizon Scales with VLBI Ground Arrays. *Bull. Am. Astron. Soc.* **2019**, *51*, 256.
40. Pesce, D.W.; Palumbo, D.C.M.; Narayan, R.; Blackburn, L.; Doeleman, S.S.; Johnson, M.D.; Ma, C.P.; Nagar, N.M.; Natarajan, P.; Ricarte, A. Toward Determining the Number of Observable Supermassive Black Hole Shadows. *Astrophys. J.* **2021**, *923*, 260. [[CrossRef](#)]
41. Cappellari, M.; Verolme, E.K.; van der Marel, R.P.; Verdoes Kleijn, G.A.; Illingworth, G.D.; Franx, M.; Carollo, C.M.; de Zeeuw, P.T. The Counterrotating Core and the Black Hole Mass of IC 1459. *Astrophys. J.* **2002**, *578*, 787–805. [[CrossRef](#)]
42. Graham, A.W. Populating the Galaxy Velocity Dispersion - Supermassive Black Hole Mass Diagram: A Catalogue of ( $M_{bh}$ ,  $\sigma$ ) Values. *Publ. Astron. Soc. Aust.* **2008**, *25*, 167–175. [[CrossRef](#)]

43. Lo, W.P.; Physics, National Taiwan University; Institute of Astronomy & Astrophysics, Taipei Taiwan; Academia Sinica, Taipei, Taiwan. Flux Density Survey of Low-Luminosity Active Galactic Nuclei at mm/submm wavelengths. 2023, *manuscript in preparation*.
44. Janssen, M.; Falcke, H.; Kadler, M.; Ros, E.; Wielgus, M.; Akiyama, K.; Baloković, M.; Blackburn, L.; Bouman, K.L.; Chael, A.; et al. Event Horizon Telescope observations of the jet launching and collimation in Centaurus A. *Nature Astron.* **2021**, *5*, 1017–1028. [[CrossRef](#)]
45. Harris, G.L.H.; Rejkuba, M.; Harris, W.E. The Distance to NGC 5128 (Centaurus A). *Publ. Astron. Soc. Aust.* **2010**, *27*, 457–462. [[CrossRef](#)]
46. Paraschos, G.F.; Kim, J.Y.; Krichbaum, T.P.; Zensus, J.A. Pinpointing the jet apex of 3C 84. *Astron. Astrophys.* **2021**, *650*, L18. [[CrossRef](#)]
47. Giovannini, G.; Savolainen, T.; Orienti, M.; Nakamura, M.; Nagai, H.; Kino, M.; Giroletti, M.; Hada, K.; Bruni, G.; Kovalev, Y.Y.; et al. A wide and collimated radio jet in 3C84 on the scale of a few hundred gravitational radii. *Nature Astron.* **2018**, *2*, 472–477. [[CrossRef](#)]
48. Brenneman, L.W.; Weaver, K.A.; Kadler, M.; Tueller, J.; Marscher, A.; Ros, E.; Zensus, A.; Kovalev, Y.Y.; Aller, M.; Aller, H.; et al. Spectral Analysis of the Accretion Flow in NGC 1052 with Suzaku. *Astrophys. J.* **2009**, *698*, 528–540. [[CrossRef](#)]
49. Falcke, H.; Melia, F.; Agol, E. Viewing the Shadow of the Black Hole at the Galactic Center. *Astrophys. J. Lett.* **2000**, *528*, L13–L16. [[CrossRef](#)] [[PubMed](#)]
50. Manmoto, T. Advection-dominated Accretion Flow around a Kerr Black Hole. *Astrophys. J.* **2000**, *534*, 734–746. [[CrossRef](#)]
51. Yuan, F.; Quataert, E.; Narayan, R. Nonthermal Electrons in Radiatively Inefficient Accretion Flow Models of Sagittarius A\*. *Astrophys. J.* **2003**, *598*, 301–312. [[CrossRef](#)]
52. De Villiers, J.P.; Hawley, J.F.; Krolik, J.H. Magnetically Driven Accretion Flows in the Kerr Metric. I. Models and Overall Structure. *Astrophys. J.* **2003**, *599*, 1238–1253. [[CrossRef](#)]
53. Hirose, S.; Krolik, J.H.; De Villiers, J.P.; Hawley, J.F. Magnetically Driven Accretion Flows in the Kerr Metric. II. Structure of the Magnetic Field. *Astrophys. J.* **2004**, *606*, 1083–1097. [[CrossRef](#)]
54. De Villiers, J.P.; Hawley, J.F.; Krolik, J.H.; Hirose, S. Magnetically Driven Accretion in the Kerr Metric. III. Unbound Outflows. *Astrophys. J.* **2005**, *620*, 878–888. [[CrossRef](#)]
55. Krolik, J.H.; Hawley, J.F.; Hirose, S. Magnetically Driven Accretion Flows in the Kerr Metric. IV. Dynamical Properties of the Inner Disk. *Astrophys. J.* **2005**, *622*, 1008–1023. [[CrossRef](#)]
56. Igumenshchev, I.V.; Narayan, R.; Abramowicz, M.A. Three-dimensional Magnetohydrodynamic Simulations of Radiatively Inefficient Accretion Flows. *Astrophys. J.* **2003**, *592*, 1042–1059. [[CrossRef](#)]
57. McKinney, J.C.; Gammie, C.F. A Measurement of the Electromagnetic Luminosity of a Kerr Black Hole. *Astrophys. J.* **2004**, *611*, 977–995. [[CrossRef](#)]
58. McKinney, J.C. General relativistic magnetohydrodynamic simulations of the jet formation and large-scale propagation from black hole accretion systems. *Mon. Not. R. Astron. Soc.* **2006**, *368*, 1561–1582. [[CrossRef](#)]
59. Hawley, J.F.; Krolik, J.H. Magnetically Driven Jets in the Kerr Metric. *Astrophys. J.* **2006**, *641*, 103–116. [[CrossRef](#)]
60. Noble, S.C.; Leung, P.K.; Gammie, C.F.; Book, L.G. Simulating the emission and outflows from accretion discs. *Class. Quantum Gravity* **2007**, *24*, S259–S274. [[CrossRef](#)]
61. Tchekhovskoy, A.; McKinney, J.C.; Narayan, R. Simulations of ultrarelativistic magnetodynamic jets from gamma-ray burst engines. *Mon. Not. R. Astron. Soc.* **2008**, *388*, 551–572. [[CrossRef](#)]
62. Mościbrodzka, M.; Gammie, C.F.; Dolence, J.C.; Shiokawa, H.; Leung, P.K. Radiative Models of SGR A\* from GRMHD Simulations. *Astrophys. J.* **2009**, *706*, 497–507. [[CrossRef](#)]
63. Punsly, B.; Igumenshchev, I.V.; Hirose, S. Three-Dimensional Simulations of Vertical Magnetic Flux in the Immediate Vicinity of Black Holes. *Astrophys. J.* **2009**, *704*, 1065–1085. [[CrossRef](#)]
64. Noble, S.C.; Krolik, J.H.; Hawley, J.F. Direct Calculation of the Radiative Efficiency of an Accretion Disk Around a Black Hole. *Astrophys. J.* **2009**, *692*, 411–421. [[CrossRef](#)]
65. Tchekhovskoy, A.; Narayan, R.; McKinney, J.C. Black Hole Spin and The Radio Loud/Quiet Dichotomy of Active Galactic Nuclei. *Astrophys. J.* **2010**, *711*, 50–63. [[CrossRef](#)]
66. Tchekhovskoy, A.; Narayan, R.; McKinney, J.C. Efficient generation of jets from magnetically arrested accretion on a rapidly spinning black hole. *Mon. Not. R. Astron. Soc.* **2011**, *418*, L79–L83. [[CrossRef](#)]
67. Shiokawa, H.; Dolence, J.C.; Gammie, C.F.; Noble, S.C. Global General Relativistic Magnetohydrodynamic Simulations of Black Hole Accretion Flows: A Convergence Study. *Astrophys. J.* **2012**, *744*, 187. [[CrossRef](#)]
68. Porth, O.; Chatterjee, K.; Narayan, R.; Gammie, C.F.; Mizuno, Y.; Anninos, P.; Baker, J.G.; Bugli, M.; Chan, C.k.; Davelaar, J.; et al. The Event Horizon General Relativistic Magnetohydrodynamic Code Comparison Project. *Astrophys. J. Suppl. Ser.* **2019**, *243*, 26. [[CrossRef](#)]
69. Martí, J.M. Numerical Simulations of Jets from Active Galactic Nuclei. *Galaxies* **2019**, *7*, 24. [[CrossRef](#)]
70. Takahashi, M.; Nitta, S.; Tatematsu, Y.; Tomimatsu, A. Magnetohydrodynamic Flows in Kerr Geometry: Energy Extraction from Black Holes. *Astrophys. J.* **1990**, *363*, 206. [[CrossRef](#)]
71. Blandford, R.D.; Znajek, R.L. Electromagnetic extraction of energy from Kerr black holes. *Mon. Not. R. Astron. Soc.* **1977**, *179*, 433–456. [[CrossRef](#)]

72. Pu, H.Y.; Nakamura, M.; Hirotani, K.; Mizuno, Y.; Wu, K.; Asada, K. Steady General Relativistic Magnetohydrodynamic Inflow/Outflow Solution Along Large-Scale Magnetic Fields that Thread a Rotating Black Hole. *Astrophys. J.* **2015**, *801*, 56. [[CrossRef](#)]
73. Lyubarsky, Y.E. Transformation of the Poynting flux into kinetic energy in relativistic jets. *Mon. Not. R. Astron. Soc.* **2010**, *402*, 353–361. [[CrossRef](#)]
74. Takahashi, M.; Tomimatsu, A. Constraints on the evolution of black hole spin due to magnetohydrodynamic accretion. *Phys. Rev. D* **2008**, *78*, 023012. [[CrossRef](#)]
75. Pu, H.Y.; Takahashi, M. Properties of Trans-fast Magnetosonic Jets in Black Hole Magnetospheres. *Astrophys. J.* **2020**, *892*, 37. [[CrossRef](#)]
76. Chatterjee, K.; Liska, M.; Tchekhovskoy, A.; Markoff, S.B. Accelerating AGN jets to parsec scales using general relativistic MHD simulations. *Mon. Not. R. Astron. Soc.* **2019**, *490*, 2200–2218. [[CrossRef](#)]
77. Narayan, R.; Igumenshchev, I.V.; Abramowicz, M.A. Magnetically Arrested Disk: An Energetically Efficient Accretion Flow. *Publ. Astron. Soc. Jpn.* **2003**, *55*, L69–L72. [[CrossRef](#)]
78. Igumenshchev, I.V. Magnetically Arrested Disks and the Origin of Poynting Jets: A Numerical Study. *Astrophys. J.* **2008**, *677*, 317–326. [[CrossRef](#)]
79. McKinney, J.C.; Tchekhovskoy, A.; Blandford, R.D. General relativistic magnetohydrodynamic simulations of magnetically choked accretion flows around black holes. *Mon. Not. R. Astron. Soc.* **2012**, *423*, 3083–3117. [[CrossRef](#)]
80. Narayan, R.; Chael, A.; Chatterjee, K.; Ricarte, A.; Curd, B. Jets in magnetically arrested hot accretion flows: geometry, power, and black hole spin-down. *Mon. Not. R. Astron. Soc.* **2022**, *511*, 3795–3813. [[CrossRef](#)]
81. Narayan, R.; Sądowski, A.; Penna, R.F.; Kulkarni, A.K. GRMHD simulations of magnetized advection-dominated accretion on a non-spinning black hole: role of outflows. *Mon. Not. R. Astron. Soc.* **2012**, *426*, 3241–3259. [[CrossRef](#)]
82. Sądowski, A.; Narayan, R.; Penna, R.; Zhu, Y. Energy, momentum and mass outflows and feedback from thick accretion discs around rotating black holes. *Mon. Not. R. Astron. Soc.* **2013**, *436*, 3856–3874. [[CrossRef](#)]
83. Mościbrodzka, M.; Falcke, H. Coupled jet-disk model for Sagittarius A\*: Explaining the flat-spectrum radio core with GRMHD simulations of jets. *Astron. Astrophys.* **2013**, *559*, L3. [[CrossRef](#)]
84. Chan, C.K.; Psaltis, D.; Özel, F.; Narayan, R.; Sądowski, A. The Power of Imaging: Constraining the Plasma Properties of GRMHD Simulations using EHT Observations of Sgr A\*. *Astrophys. J.* **2015**, *799*, 1. [[CrossRef](#)]
85. Dexter, J.; Agol, E.; Fragile, P.C.; McKinney, J.C. The Submillimeter Bump in Sgr A\* from Relativistic MHD Simulations. *Astrophys. J.* **2010**, *717*, 1092–1104. [[CrossRef](#)]
86. Chael, A.; Rowan, M.; Narayan, R.; Johnson, M.; Sironi, L. The role of electron heating physics in images and variability of the Galactic Centre black hole Sagittarius A\*. *Mon. Not. R. Astron. Soc.* **2018**, *478*, 5209–5229. [[CrossRef](#)]
87. Chael, A.; Narayan, R.; Johnson, M.D. Two-temperature, Magnetically Arrested Disc simulations of the jet from the supermassive black hole in M87. *Mon. Not. R. Astron. Soc.* **2019**, *486*, 2873–2895. [[CrossRef](#)]
88. Davelaar, J.; Mościbrodzka, M.; Bronzwaer, T.; Falcke, H. General relativistic magnetohydrodynamical  $\kappa$ -jet models for Sagittarius A\*. *Astron. Astrophys.* **2018**, *612*, A34. [[CrossRef](#)]
89. Davelaar, J.; Olivares, H.; Porth, O.; Bronzwaer, T.; Janssen, M.; Roelofs, F.; Mizuno, Y.; Fromm, C.M.; Falcke, H.; Rezzolla, L. Modeling non-thermal emission from the jet-launching region of M 87 with adaptive mesh refinement. *Astron. Astrophys.* **2019**, *632*, A2. [[CrossRef](#)]
90. Cruz-Ororio, A.; Fromm, C.M.; Mizuno, Y.; Nathanail, A.; Younsi, Z.; Porth, O.; Davelaar, J.; Falcke, H.; Kramer, M.; Rezzolla, L. State-of-the-art energetic and morphological modelling of the launching site of the M87 jet. *Nature Astronomy* **2022**, *6*, 103–108. [[CrossRef](#)]
91. Chael, A.A.; Narayan, R.; Sądowski, A. Evolving non-thermal electrons in simulations of black hole accretion. *Mon. Not. R. Astron. Soc.* **2017**, *470*, 2367–2386. [[CrossRef](#)]
92. Beskin, V.S. *MHD Flows in Compact Astrophysical Objects: Accretion, Winds and Jets*; Springer: Berlin/Heidelberg, Germany, 2009.
93. Fendt, C.; Camenzind, M.; Appl, S. On the collimation of stellar magnetospheres to jets. I. Relativistic force-free 2D equilibrium. *Astron. Astrophys.* **1995**, *300*, 791.
94. Pan, Z.; Yu, C.; Huang, L. Analytic Properties of Force-free Jets in the Kerr Spacetime. III. Uniform Field Solution. *Astrophys. J.* **2017**, *836*, 193. [[CrossRef](#)]
95. Huang, L.; Pan, Z.; Yu, C. Toward a Full MHD Jet Model of Spinning Black Holes. I. Framework and a Split Monopole Example. *Astrophys. J.* **2019**, *880*, 93. [[CrossRef](#)]
96. Asada, K.; Nakamura, M. The Structure of the M87 Jet: A Transition from Parabolic to Conical Streamlines. *Astrophys. J. Lett.* **2012**, *745*, L28. [[CrossRef](#)]
97. Nakamura, M.; Asada, K. The Parabolic Jet Structure in M87 as a Magnetohydrodynamic Nozzle. *Astrophys. J.* **2013**, *775*, 118. [[CrossRef](#)]
98. Nakamura, M.; Asada, K.; Hada, K.; Pu, H.Y.; Noble, S.; Tseng, C.; Toma, K.; Kino, M.; Nagai, H.; Takahashi, K.; et al. Parabolic Jets from the Spinning Black Hole in M87. *Astrophys. J.* **2018**, *868*, 146. [[CrossRef](#)]
99. Broderick, A.E.; Loeb, A. Imaging the Black Hole Silhouette of M87: Implications for Jet Formation and Black Hole Spin. *Astrophys. J.* **2009**, *697*, 1164–1179. [[CrossRef](#)]

100. Narayan, R.; McKinney, J.C.; Farmer, A.J. Self-similar force-free wind from an accretion disc. *Mon. Not. R. Astron. Soc.* **2007**, *375*, 548–566. [[CrossRef](#)]
101. Lu, R.S.; Broderick, A.E.; Baron, F.; Monnier, J.D.; Fish, V.L.; Doeleman, S.S.; Pankratius, V. Imaging the Supermassive Black Hole Shadow and Jet Base of M87 with the Event Horizon Telescope. *Astrophys. J.* **2014**, *788*, 120. [[CrossRef](#)]
102. Mościbrodzka, M.; Dexter, J.; Davelaar, J.; Falcke, H. Faraday rotation in GRMHD simulations of the jet launching zone of M87. *Mon. Not. R. Astron. Soc.* **2017**, *468*, 2214–2221. [[CrossRef](#)]
103. Jeter, B.; Broderick, A.E.; Gold, R. Differentiating disc and black hole-driven jets with EHT images of variability in M87. *Mon. Not. R. Astron. Soc.* **2020**, *493*, 5606–5616. [[CrossRef](#)]
104. Takahashi, K.; Toma, K.; Kino, M.; Nakamura, M.; Hada, K. Fast-spinning Black Holes Inferred from Symmetrically Limb-brightened Radio Jets. *Astrophys. J.* **2018**, *868*, 82. [[CrossRef](#)]
105. Ogihara, T.; Takahashi, K.; Toma, K. A Mechanism for the Triple-ridge Emission Structure of AGN Jets. *Astrophys. J.* **2019**, *877*, 19. [[CrossRef](#)]
106. Camenzind, M. Centrifugally driven MHD-winds in active galactic nuclei. *Astron. Astrophys.* **1986**, *156*, 137–151.
107. Camenzind, M. Hydromagnetic flows from rapidly rotating compact objects. I—Cold relativistic flows from rapid rotators. *Astron. Astrophys.* **1986**, *162*, 32–44.
108. Camenzind, M. Hydromagnetic flows from rapidly rotating compact objects. II—The relativistic axisymmetric jet equilibrium. *Astron. Astrophys.* **1987**, *184*, 341–360.
109. Fendt, C.; Camenzind, M. On collimated stellar jet magnetospheres. II. Dynamical structure of collimating wind flows. *Astron. Astrophys.* **1996**, *313*, 591–604.
110. Fendt, C.; Greiner, J. Magnetically driven superluminal motion from rotating black holes. Solution of the magnetic wind equation in Kerr metric. *Astron. Astrophys.* **2001**, *369*, 308–322. [[CrossRef](#)]
111. Fendt, C.; Ouyed, R. Ultrarelativistic Magnetohydrodynamic Jets in the Context of Gamma-Ray Bursts. *Astrophys. J.* **2004**, *608*, 378–390. [[CrossRef](#)]
112. Pu, H.Y.; Hirofani, K.; Chang, H.K. Launching and Quenching of Black Hole Relativistic Jets at Low Accretion Rate. *Astrophys. J.* **2012**, *758*, 113. [[CrossRef](#)]
113. Beskin, V.S.; Kuznetsova, I.V.; Rafikov, R.R. On the MHD effects on the force-free monopole outflow. *Mon. Not. R. Astron. Soc.* **1998**, *299*, 341–348. [[CrossRef](#)]
114. Beskin, V.S.; Nokhrina, E.E. The effective acceleration of plasma outflow in the paraboloidal magnetic field. *Mon. Not. R. Astron. Soc.* **2006**, *367*, 375–386. [[CrossRef](#)]
115. Tomimatsu, A.; Takahashi, M. Relativistic Acceleration of Magnetically Driven Jets. *Astrophys. J.* **2003**, *592*, 321–331. [[CrossRef](#)]
116. Ogihara, T.; Ogawa, T.; Toma, K. Matter Density Distribution of General Relativistic Highly Magnetized Jets Driven by Black Holes. *Astrophys. J.* **2021**, *911*, 34. [[CrossRef](#)]
117. Dexter, J.; McKinney, J.C.; Agol, E. The size of the jet launching region in M87. *Mon. Not. R. Astron. Soc.* **2012**, *421*, 1517–1528. [[CrossRef](#)]
118. Balbus, S.A.; Hawley, J.F. A Powerful Local Shear Instability in Weakly Magnetized Disks. I. Linear Analysis. *Astrophys. J.* **1991**, *376*, 214. [[CrossRef](#)]
119. O’Riordan, M.; Pe’er, A.; McKinney, J.C. Observational Signatures of Mass-loading in Jets Launched by Rotating Black Holes. *Astrophys. J.* **2018**, *853*, 44. [[CrossRef](#)]
120. Leung, P.K.; Gammie, C.F.; Noble, S.C. Numerical Calculation of Magnetobremstrahlung Emission and Absorption Coefficients. *Astrophys. J.* **2011**, *737*, 21. [[CrossRef](#)]
121. Pandya, A.; Zhang, Z.; Chandra, M.; Gammie, C.F. Polarized Synchrotron Emissivities and Absorptivities for Relativistic Thermal, Power-law, and Kappa Distribution Functions. *Astrophys. J.* **2016**, *822*, 34. [[CrossRef](#)]
122. Dexter, J. A public code for general relativistic, polarised radiative transfer around spinning black holes. *Mon. Not. R. Astron. Soc.* **2016**, *462*, 115–136. [[CrossRef](#)]
123. Özel, F.; Psaltis, D.; Narayan, R. Hybrid Thermal-Nonthermal Synchrotron Emission from Hot Accretion Flows. *Astrophys. J.* **2000**, *541*, 234–249. [[CrossRef](#)]
124. Fromm, C.M.; Cruz-Ororio, A.; Mizuno, Y.; Nathanail, A.; Younsi, Z.; Porth, O.; Olivares, H.; Davelaar, J.; Falcke, H.; Kramer, M.; et al. Impact of non-thermal particles on the spectral and structural properties of M87. *Astron. Astrophys.* **2022**, *660*, A107. [[CrossRef](#)]
125. Fuerst, S.V.; Wu, K. Radiation transfer of emission lines in curved space-time. *Astron. Astrophys.* **2004**, *424*, 733–746. [[CrossRef](#)]
126. Younsi, Z.; Wu, K.; Fuerst, S.V. General relativistic radiative transfer: Formulation and emission from structured tori around black holes. *Astron. Astrophys.* **2012**, *545*, A13. [[CrossRef](#)]
127. Gold, R.; Broderick, A.E.; Younsi, Z.; Fromm, C.M.; Gammie, C.F.; Mościbrodzka, M.; Pu, H.Y.; Bronzwaer, T.; Davelaar, J.; Dexter, J.; et al. Verification of Radiative Transfer Schemes for the EHT. *Astrophys. J.* **2020**, *897*, 148. [[CrossRef](#)]
128. Broderick, A.E.; McKinney, J.C. Parsec-scale Faraday Rotation Measures from General Relativistic Magnetohydrodynamic Simulations of Active Galactic Nucleus Jets. *Astrophys. J.* **2010**, *725*, 750–773. [[CrossRef](#)]
129. Chatterjee, K.; Markoff, S.; Neilsen, J.; Younsi, Z.; Witzel, G.; Tchekhovskoy, A.; Yoon, D.; Ingram, A.; van der Klis, M.; Boyce, H.; et al. General relativistic MHD simulations of non-thermal flaring in Sagittarius A\*. *Mon. Not. R. Astron. Soc.* **2021**, *507*, 5281–5302. [[CrossRef](#)]

130. Gammie, C.F.; McKinney, J.C.; Tóth, G. HARM: A Numerical Scheme for General Relativistic Magnetohydrodynamics. *Astrophys. J.* **2003**, *589*, 444–457. [[CrossRef](#)]
131. Noble, S.C.; Gammie, C.F.; McKinney, J.C.; Del Zanna, L. Primitive Variable Solvers for Conservative General Relativistic Magnetohydrodynamics. *Astrophys. J.* **2006**, *641*, 626–637. [[CrossRef](#)]
132. Pu, H.Y.; Yun, K.; Younsi, Z.; Yoon, S.J. Odyssey: A Public GPU-based Code for General Relativistic Radiative Transfer in Kerr Spacetime. *Astrophys. J.* **2016**, *820*, 105. [[CrossRef](#)]
133. Mościbrodzka, M.; Falcke, H.; Shiokawa, H. General relativistic magnetohydrodynamical simulations of the jet in M 87. *Astron. Astrophys.* **2016**, *586*, A38. [[CrossRef](#)]
134. Ball, D.; Sironi, L.; Özel, F. Electron and Proton Acceleration in Trans-relativistic Magnetic Reconnection: Dependence on Plasma Beta and Magnetization. *Astrophys. J.* **2018**, *862*, 80. [[CrossRef](#)]
135. Ball, D.; Özel, F.; Psaltis, D.; Chan, C.K. Particle Acceleration and the Origin of X-Ray Flares in GRMHD Simulations of SGR A. *Astrophys. J.* **2016**, *826*, 77. [[CrossRef](#)]
136. Broderick, A.E.; Tchekhovskoy, A. Horizon-scale Lepton Acceleration in Jets: Explaining the Compact Radio Emission in M87. *Astrophys. J.* **2015**, *809*, 97. [[CrossRef](#)]
137. Pu, H.Y.; Wu, K.; Younsi, Z.; Asada, K.; Mizuno, Y.; Nakamura, M. Observable Emission Features of Black Hole GRMHD Jets on Event Horizon Scales. *Astrophys. J.* **2017**, *845*, 160. [[CrossRef](#)]
138. Kawashima, T.; Toma, K.; Kino, M.; Akiyama, K.; Nakamura, M.; Moriyama, K. A Jet-bases Emission Model of the EHT2017 Image of M87\*. *Astrophys. J.* **2021**, *909*, 168. [[CrossRef](#)]
139. Ressler, S.M.; Tchekhovskoy, A.; Quataert, E.; Chandra, M.; Gammie, C.F. Electron thermodynamics in GRMHD simulations of low-luminosity black hole accretion. *Mon. Not. R. Astron. Soc.* **2015**, *454*, 1848–1870. [[CrossRef](#)]
140. Ryan, B.R.; Dolence, J.C.; Gammie, C.F. bhlight: General Relativistic Radiation Magnetohydrodynamics with Monte Carlo Transport. *Astrophys. J.* **2015**, *807*, 31. [[CrossRef](#)]
141. Sądowski, A.; Wielgus, M.; Narayan, R.; Abarca, D.; McKinney, J.C.; Chael, A. Radiative, two-temperature simulations of low-luminosity black hole accretion flows in general relativity. *Mon. Not. R. Astron. Soc.* **2017**, *466*, 705–725. [[CrossRef](#)]
142. Ressler, S.M.; Tchekhovskoy, A.; Quataert, E.; Gammie, C.F. The disc-jet symbiosis emerges: Modelling the emission of Sagittarius A\* with electron thermodynamics. *Mon. Not. R. Astron. Soc.* **2017**, *467*, 3604–3619. [[CrossRef](#)]
143. Ryan, B.R.; Ressler, S.M.; Dolence, J.C.; Gammie, C.; Quataert, E. Two-temperature GRRMHD Simulations of M87. *Astrophys. J.* **2018**, *864*, 126. [[CrossRef](#)]
144. Liska, M.; Hesp, C.; Tchekhovskoy, A.; Ingram, A.; van der Klis, M.; Markoff, S. Formation of precessing jets by tilted black hole discs in 3D general relativistic MHD simulations. *Mon. Not. R. Astron. Soc.* **2018**, *474*, L81–L85. [[CrossRef](#)]
145. White, C.J.; Quataert, E.; Blaes, O. Tilted Disks around Black Holes: A Numerical Parameter Survey for Spin and Inclination Angle. *Astrophys. J.* **2019**, *878*, 51. [[CrossRef](#)]
146. Liska, M.; Hesp, C.; Tchekhovskoy, A.; Ingram, A.; van der Klis, M.; Markoff, S.B. A Phase Lag between Disk and Corona in GRMHD Simulations of Precessing Tilted Accretion Disks. *arXiv* **2019**, arXiv:1901.05970.
147. Chatterjee, K.; Younsi, Z.; Liska, M.; Tchekhovskoy, A.; Markoff, S.B.; Yoon, D.; van Eijnatten, D.; Hesp, C.; Ingram, A.; van der Klis, M.B.M. Observational signatures of disc and jet misalignment in images of accreting black holes. *Mon. Not. R. Astron. Soc.* **2020**, *499*, 362–378. [[CrossRef](#)]
148. Liska, M.; Hesp, C.; Tchekhovskoy, A.; Ingram, A.; van der Klis, M.; Markoff, S.B.; Van Moer, M. Disc tearing and Bardeen-Petterson alignment in GRMHD simulations of highly tilted thin accretion discs. *Mon. Not. R. Astron. Soc.* **2021**, *507*, 983–990. [[CrossRef](#)]
149. Mościbrodzka, M.; Gammie, C.F.; Dolence, J.C.; Shiokawa, H. Pair Production in Low-luminosity Galactic Nuclei. *Astrophys. J.* **2011**, *735*, 9. [[CrossRef](#)]
150. Emami, R.; Anantua, R.; Chael, A.A.; Loeb, A. Positron Effects on Polarized Images and Spectra from Jet and Accretion Flow Models of M87\* and Sgr A\*. *Astrophys. J.* **2021**, *923*, 272. [[CrossRef](#)]
151. Wong, G.N.; Ryan, B.R.; Gammie, C.F. Pair Drizzle around Sub-Eddington Supermassive Black Holes. *Astrophys. J.* **2021**, *907*, 73. [[CrossRef](#)]
152. Mizuno, Y. GRMHD Simulations and Modeling for Jet Formation and Acceleration Region in AGNs. *Universe* **2022**, *8*, 85. [[CrossRef](#)]
153. Ricarte, A.; Qiu, R.; Narayan, R. Black hole magnetic fields and their imprint on circular polarization images. *Mon. Not. R. Astron. Soc.* **2021**, *505*, 523–539. [[CrossRef](#)]